Journal of Alloys and Compounds 805 (2019) 779–788

Contents lists available at ScienceDirect

Journal of Alloys and Compounds

journal homepage: http://www.elsevier.com/locate/jalcom

Synthesis, structure, and properties of $EuErCuS_3$

Anna V. Ruseikina [a, *], Leonid A. Solovyov [b], Vladimir A. Chernyshev [c], Aleksandr S. Aleksandrovsky [d, e], Oleg V. Andreev [a], Svetlana N. Krylova [d], Alexander S. Krylov [d], Dmitriy A. Velikanov [d], Maxim S. Molokeev [f, g], Nikolai G. Maximov [h], Maxim V. Grigoriev [a], Alexander A. Garmonov [i], Alexey V. Matigorov [a]

[a] Institute of Chemistry, University of Tyumen, Tyumen, 625003, Russia
[b] Institute of Chemistry and Chemical Technology, Federal Research Center KSC SB RAS, Krasnoyarsk, 660049, Russia
[c] Institute of Natural Sciences and Mathematics, Ural Federal University, Ekaterinburg, 620002, Russia
[d] Laboratory of Coherent Optics, Kirensky Institute of Physics, Federal Research Center KSC SB RAS, Krasnoyarsk, 660036, Russia
[e] Department of Photonics and Laser Technologies, Siberian Federal University, Krasnoyarsk, 660079, Russia
[f] Laboratory of Crystal Physics, Kirensky Institute of Physics, Federal Research Center KSC SB RAS, Krasnoyarsk, 660036, Russia
[g] Siberian Federal University, Krasnoyarsk, 660079, Russia
[h] Institute of Chemistry and Chemical Technology SB RAS, Federal Research Center "Krasnoyarsk Science Center SB RAS", Russia
[i] Institute of Physics and Technology, University of Tyumen, Tyumen, 625003, Russia

ARTICLE INFO

Article history:
Received 19 May 2019
Received in revised form
29 June 2019
Accepted 5 July 2019
Available online 12 July 2019

Keywords:
Inorganic materials
Thermochemistry
Spectroscopy
Magnetic measurements
Optical spectroscopy
X-ray diffraction

ABSTRACT

The crystal structure of the first-synthesized compound $EuErCuS_3$ was determined from X-ray powder diffraction data: orthorhombic crystal system, space group *Pnma*, structural type Eu_2CuS_3: a = 10.1005(2) Å, b = 3.91255(4)Å, c = 12.8480(2) Å; V = 507.737(14) Å^3, Z = 4, and $\rho_x = 6.266$ g/cm^3. The temperatures and enthalpies of reversible polymorphic transitions and incongruent melting of the compound were determined by DSC: $T_{\alpha\leftrightarrow\beta} = 1524$ K, $\Delta H_{\alpha\leftrightarrow\beta} = 2.3 \pm 0.2$ kJ·mol^{-1}; $T_{\beta\leftrightarrow\gamma} = 1575$ K, $\Delta H_{\beta\leftrightarrow\gamma} = 0.7 \pm 0.1$ kJ·mol^{-1}; $T_{\gamma\leftrightarrow\delta} = 1602$ K; $\Delta H_{\gamma\leftrightarrow\delta} = 1.3 \pm 0.1$ kJ·mol^{-1} and $T_{cr} = 1735 \pm 10$ K, $\Delta H_{cr} = -3.5 \pm 0.3$ kJ·mol^{-1}. IR spectra were recorded in the range from 50 to 400 cm^{-1}. The compound was found to be IR-transparent in the range 4000–400 cm^{-1}. The compound was characterized by Raman spectroscopy. The observed spectra featured both Raman lines and luminescence. Ab initio calculations of the $EuErCuS_3$ crystal structure and phonon spectrum were performed, the frequencies and types of fundamental modes were determined, and the involvement of constituent ions in the IR and Raman modes was assessed from an analysis of the ab initio displacement vectors. The vibrational spectra were interpreted. $EuErCuS_3$ manifests a ferrimagnetic transition at 4.8 K. Its microhardness is 2850 MPa. The obtained data can serve as the basis for predicting the properties of $EuLnCuS_3$ compounds. Valence states for Eu (2+) and Er (3+) are proved both by the XRD and optical methods. Optical band gap was found to be 1.934 eV from diffuse reflectance spectrum.

1. Introduction

Triple and quadruple chalcogenides of rare-earth elements have been intensively studied in recent years due to their specific properties, which make them promising materials in the field of infrared and nonlinear optics [1]. They are important as refractory materials with semiconducting properties and promise high temperature superconductors [2]. Synthesis and study of the crystal structures of complex chalcogenides is an important step in the search for new materials with desirable properties [1].

Complex rare-earth chalcogenides $ALnCuS_3$ and ALn_3CuS_6 (A^{2+} = Pb, Eu, Sr, or Ba) have specific electric [1–7], thermal [8–12], magnetic [1,13–15], and optical [1,9,12,15] properties. X-ray powder diffraction analyses of the samples annealed at 1170 K indicated three types of orthorhombic crystal structures in the $EuLnCuS_3$ (Ln = La–Ho, Tm–Lu) series [13,16,17] (Table 1).

* Corresponding author. Institute of Chemistry, University of Tyumen, Perekopskaya 15a, Tyumen, 625003, Russia. Tel.: +7 3452 59 74 00.
E-mail address: a.v.rusejkina@utmn.ru (A.V. Ruseikina).

https://doi.org/10.1016/j.jallcom.2019.07.059
0925-8388/

Table 1
The structural types (STs) of $EuLnCuS_3$ (Ln = La–Lu) compounds were determined in the samples annealed at 1170 K.2

$EuLnCuS_3$ structural type											
La	Ce	Pr	Nd	Sm	Gd	Tb	Dy	Ho	Er	Tm	Yb	Lu
									-			

The background cell coloring denotes the structural type (ST) in which the $EuLnCuS_3$ compound crystallizes: crosshatched cells – Eu_2CuS_3 ST, dark gray cells – Ba_2MnS_3 ST, horizontal-striped cells – $KZrCuS_3$ ST, and hyphenated white cells – an undetermined ST.

The $EuLnCuS_3$ (Ln = Tb, Dy, and Tm) compounds that contain magnetic Ln^{3+} ions manifest a ferrimagnetic transition at 5.4, 5.3, and 5.4 K, respectively; in the compounds containing nonmagnetic Ln^{3+}ions (Ln = Y, Eu, and Lu), ferromagnetic ordering of Eu^{2+} moments takes place at 3.4–4.4 K [13,14].

The $ALnCuS_3$ (A = Sr, Eu; Ln = Gd, Dy, and Ho) compounds manifest three polymorphic transitions at temperatures above 1400 K upon heating and cooling as shown by differential scanning calorimetry (DSC) [8,18,19]. For $EuHoCuS_3$, the polymorphic transition temperatures and enthalpies are $T_{\alpha\leftrightarrow\beta} = 1516$ K, $\Delta H_{\alpha\leftrightarrow\beta} = 3.7$ kJ/mol; $T_{\beta\leftrightarrow\gamma} = 1562$ K, $\Delta H_{\beta\leftrightarrow\gamma} = 1.2$ kJ/mol; and $T_{\gamma\leftrightarrow\delta} = 1591$ K, $\Delta H_{\gamma\leftrightarrow\delta} = 2.2$ kJ/mol [18]. High-temperature polymorphs have not been obtained by cooling or quenching. The $EuLnCuS_3$ compounds melt incongruently: $EuLaCuS_3$ (1539 ± 4 K), $EuCeCuS_3$ (1524 ± 3 K), $EuPrCuS_3$ (1497 ± 3 K), $EuNdCuS_3$ (1470±4K) [9,17]), $EuGdCuS_3$ (1720 ± 5 K) [8], $EuHoCuS_3$ (1721 ± 5 K) [18] and $EuDyCuS_3$ (1721±4K) [19].

We failed to find any piece of data on the crystal structure, thermal, optical, or magnetic properties of $EuErCuS_3$ in the literature. The lack of data related to the properties and physicochemical characteristics of the compound $EuErCuS_3$ limits the definite anticipation of potential fields of its practical application.

The purposes of this research were: first, to prepare the compound $EuErCuS_3$ and determine its structure, second, to characterize it by physicochemical methods, third, to determine its optical and magnetic properties. The special goal is related to the verification of valence states of two rare earth ions, Eu and Er in the crystal structure under investigation. It is known that most stable valence of RE ions is 3+, and if no precautions are taken, they tend to attain this valence state even while occupying sites with nominal valence 2+, due to inclusion of, e.g, oxygen-containing defects, like in the case of doping of fluorite crystals with RE. Some hosts are especially favorable for stabilizing divalent RE ions like single crystalline alpha-SBO doped with europium. In the case of the crystal structure under consideration, i.e., $EuErCuS_3$, the competition between Eu and Er for occupying either divalent or trivalent positions may be of interest. It must be noted that in earlier studied compounds (see references above) Eu is found to be in divalent state, in accordance with the additional stability of f^7 shell of Eu^{2+} ion. In the compound under study the investigation of valence states of RE ions can be done with the help of XRD or optical spectroscopy.

2. Experimental

The compound $EuErCuS_3$ was prepared by alloying a batch of composition 2EuS: $1Er_2S_3$: $1Cu_2S$ [17–19]. Cu_2S was prepared by heating the constituent elements (Cu (99.99%, Red Chemist, Ltd., Russia) and S (99.99%, the manufacturer is Komponent-reactive, Russia)) to 1420 K for 24 h in an evacuated and sealed-off double-walled silica glass ampoule, followed by 30-min isothermal exposure at the same temperature. The Cu_2S sample prepared by the technique, described above is orthorhombic, space group is *Ab2m* [20], with the unit cell parameters $a = 13.53(3)$ Å, $b = 27.47(3)$ Å, $c = 11.88(1)$ Å. The DSC curves for this sample featured peaks that corresponded to the polymorphic transitions α-$Cu_2S \rightarrow \beta$-Cu_2S at 376 K and β-$Cu_2S \rightarrow \gamma$-Cu_2S at 708 K and the melting peak of the compound at 1402 K, in accordance with the research data [21]. Single-phase EuS and Er_2S_3 samples were prepared from Ln_2O_3 (99.99%, Red Chemist, Ltd., Russia) in the H_2S and CS_2 flow at 1300 K [16,22–24]. δ-Er_2S_3 is a monoclinic compound, space group is $P2_1/m$ [25,26], with $a = 17.42(2)$ Å, $b = 3.976(4)$ Å, $c = 10.04(1)$ Å, $\beta = 98.5(5)^\circ$. EuS is cubic, space group is *Fm3m* [27,28], with $a = 5.968(1)$ Å. According to the data of energy dispersive X-ray spectrometric analysis, the ratio of the rare-earth element and sulfur is $m_{found}(Eu) = 82.7(7)$ mass. %, $m_{found}(S) = 17.3(2)$ mass. % and $m_{found}(Er) = 78.0(8)$ mass. %, $m_{found}(S) = 21.7(2)$ mass. % respectively. The oxygen content in the test portion of the sample Er_2S_3 was 0.3 mass. %.

A 2EuS: $1Er_2S_3$:$1Cu_2S$ batch was pounded in an agate mortar and then alloyed in a graphite crucible placed inside an argon (99.998%, the manufacturer of technical gases is “Kislorod-servis”, Russia)-filled silica glass reactor, or in an evacuate and sealed-off silica glass ampoule. The synthesized samples were annealed in evacuated and sealed-off silica glass ampoules at 1170 K for 1500 h [16,29].

X-ray diffraction experiments were carried out by means of a DRON-7 diffractometer and a PANalytical X'Pert PRO diffractometer both equipped with a PIXcel detector (Fe-filtered CoK_α radiation). The X-ray diffraction patterns were scanned at 298 K over the angle range $10^\circ \leq 2\theta \leq 125(145)$ with 0.013° steps; the total accumulation time was 13 h. Unit cell parameters were determined by the ITO program [30]. Apart from the major phase, the refined model included identified microimpurities: 1 mass. % Er_2O_2S. Phase identification was with reference to the ICDDPDF4+2012 file. The observed systematic absences showed that the $EuErCuS_3$ structure (after annealing at 1170 K) belongs to space group *Pnma* (for general reflections hkl, no systematic absences were observed, so the unit cell is primitive; for reflections 0 kl: k + l = 2n; for hk0: h = 2n; for h00: h = 2n; for 0k0: k = 2n; and for 00l: l = 2n). The dataset for the isostructural compound Eu_2CuS_3 was used as reference model [31]. The crystal structure was specified by the difference derivative minimization (DDM) method [32] in the anisotropic approximation for all atoms with account for preferred orientation, anisotropic peak broadening, surface roughness and displacement ($R_{DDM} = 5.3\%$; $R_{Bragg} = 2.9\%$). The crystallographic data are referred to the data in Cambridge Crystallographic Data Centre (CCDC # 1911666), that can be downloaded from the site (www.ccdc.cam.ac.uk/data_request/cif). Crystal structures were visualized in the program package Diamond 3 [33].

The microstructural analysis of the polished samples was performed by means of metallographical microscope AxioVert.A1.

Scanning electron microscopy (SEM) was performed on a JEOLJSM-6510 LV equipped with an energy dispersive spectrometer.

Differential scanning calorimetry experiments were carried out on a Setsys Evolution 1750 (TG–DSC 1600) with the aid of the PtRh 6%-PtRh 30% thermocouple. The complex was calibrated according to the data of melting temperatures and melting enthalpies of standard substances (Sn, Pb, Zn, Al, Ag, Au, Cu, and Pd). Prior to an experiment, the working chamber of the complex was evacuated and then filled with argon. The recording parameters were the following: the sample size: 100–110 mg, heating rate: 5 K/min, argon flow rate: 25 mL/min, and alundum crucible capacity: 100 μL. The heat absorption onset temperature was determined as the intersection point of a tangent with the baseline in the program package Setsoft Software 2000 with a linear baseline from first to last point. The temperatures and enthalpies of the thermal events appearing in replica measurements are aligned with the thermoanalytical error bar. TG curves showed a 0.025 wt % weight loss in a $EuErCuS_3$ sample in the range 1678–1745 K.

A durometric analysis of a polished sample was performed by the Vickers method on an HMV-G21 [34]. The exposure time was 15 s; the load was 10 kg-force (98.07 N).

The room-temperature magnetic properties of $EuErCuS_3$ were studied on a vibrating sample magnetometer with a Puzey electromagnet [35]. The sample weight was 0.0543 g. Low-temperature magnetic susceptibility was studied on a SQUID magnetometer [36] in a 10-Oe magnetic field. Temperature-dependent magnetic susceptibility was measured in the ZFC (zero-field cooling) and FC (nonzero-field cooling) modes. A magnetic moment versus magnetic field plot for $EuErCuS_3$ was constructed by 768 datapoints in the range from 0 to 9650 Oe. The magnetic field was varied in 10–20 Oe steps.

IR spectra in the range 600–50 cm^{-1} were recorded with 2-cm^{-1} resolution on a VERTEX 70V (BRUKER) FT-IR vacuum spectrometer equipped with a SiC IR source and an RT-DTGS detector with a polyethylene window and a T240/3wide-band amplifier. Prior to measurements the spectrometer was evacuated to a residual pressure of less than 0.2 gPa. A cast complex sulfide sample was pounded in an agate mortar; the thus-prepared powder was placed on a diamond crystal of a Platinum ATR single-reflection ATR accessory for measurements.

IR absorption spectra in the range 4000–400 cm^{-1} were measured on a FTIR spectral Varian Excalibur HE 3600.

Raman spectra were excited by polarized 514.5-nm and 457.9-nm beams of a Spectra-Physics Stabilite 2017 200-mW argon laser (250 μW on the test sample). The laser beam was focused on the test sample by an Olympus BX41 updated microscope through an Olympus MPlan 100x object lens with the digital aperture 0.9. The scattered beam was collected through the same object lens and targeted to the spectrometer. Spectra in the 180° (back-scattered) geometry were obtained on a Horiba Jobin Yvon T64000 spectrometer with a triple monochromator in the dispersion subtraction mode in the frequency range 15–3600 cm^{-1}. The used detector was a liquid nitrogen-cooled CCD matrix. The focused laser beam diameter was ~2 μm.

The ab initio calculations of the $EuErCuS_3$ crystal structure and phonon spectrum were carried out in the framework of density functional theory (DFT) [37] using the B3LYP exchange-correlation functional [38,39] to take into account both local and nonlocal Hartree–Fock exchanges. The calculations were carried out in the program CRYSTAL14 [40,41]. For europium and erbium, the ECP53MWB and ECP57MWB quasi-relativistic pseudo-potentials [42,43] were used with the attached valence basis set ECP53MWB and ECP57MWB-I, respectively [44]. The Gaussian primitives with exponents less than 0.1 were removed from the basis sets. For copper, the full-electron basis set [45] was used, available on the CRYSTAL program site as « Cu_86–4111(41D)G_doll_2000» [41]. For sulfur, the DURAND pseudo-potential with the attached valence basis set was used [41,46]. The exponents in the two outer orbitals of the valence basis set were changed into 0.24 and 0.27. 125 IBZ points were used. The use of pseudo-potentials for the description of core electronic shells of rare-earth ions, the 4f shell inclusive, with the valence orbitals involved in chemical bonding described by valence basis sets, makes it possible to successfully reconstitute the lattice structure and lattice dynamics in the compounds that have a lanthanide ion sublattice [47,48]. The crystal structure was first calculated, followed by phonon spectrum calculations for crystal structure optimization. Calculation details are found elsewhere [47].

Diffuse reflection spectrum of $EuErCuS_3$ was measured using Shimadzu UV-3600 spectrometer.

3. Results and discussion

3.1. Crystal structure

The $EuErCuS_3$ diffraction pattern (Fig. 1) was indexed in terms of orthorhombic space group *Pnma*, Eu_2CuS_3 structural type, with the unit cell parameters a = 10.1005(2) Å, b = 3.91255(4) Å, c = 12.8480(2) Å; V = 507.737(14) $Å^3$, Z = 4, $\rho_x = 6.266\ g/cm^3$. The unit cell parameters calculated in the DFT frame with the B3LYP functional (a = 10.126 Å, b = 3.896 Å, c = 12.600 Å, $V = 497.044\ Å^3$) correlated with the experimental values.

The $EuErCuS_3$ structure is described by two-dimensional layers ($CuErS_3$) in plane b–a built of distorted tetrahedra CuS_4 and octahedral ErS_6, with Eu^{2+} ions in between (Fig. 2). The atomic coordinates and selected interatomic distances for $EuErCuS_3$ are listed in Table 2 and Table 3, respectively. The selected bond angles are given in Table 4.

The parenthesized values are mean interatomic distances. Symmetric positions: (i) 1 + x, y, z; (ii) 1-x, −0.5 + y, -z; (iii) 1-x, −0.5 + y, 1-z; (iv) -x, −0.5 + y, 1-z; (v) 0.5-x, -y, 0.5 + z; (vi) −0.5 + x, 0.5-y, 1.5-z; (vii) 0.5-x, -y, −0.5 + z; (viii) 1-x, 0.5 + y, -z; (ix) 1-x, 0.5 + y, 1-z; (x) -x, 0.5 + y, 1-z; (xi) 0.5-x, 1-y, 0.5 + z; and (xii) 0.5-x, 1-y, −0.5 + z.

Bond valence sum calculation is sometimes used for determination of valence states from the XRD data. Commonly it is considered as indirect method with low fidelity. Nevertheless, we

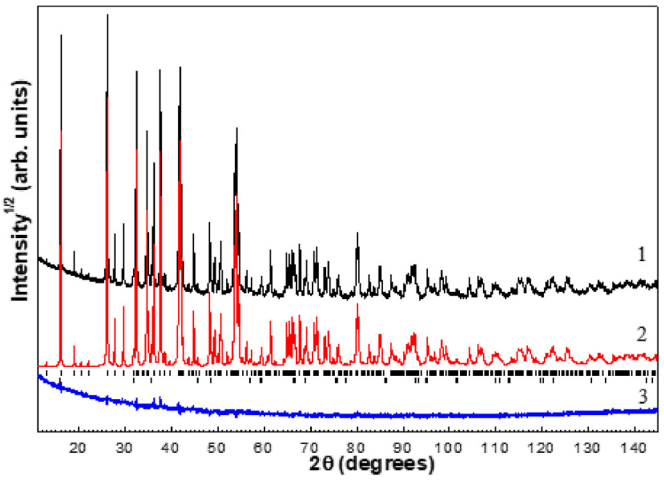

Fig. 1. Measured (1), calculated (2), and difference (3) X-ray diffraction profiles of a $EuErCuS_3$ sample after DDM structure refinement. The bars indicate the peaks positions of the major phase and Er_2O_2S.

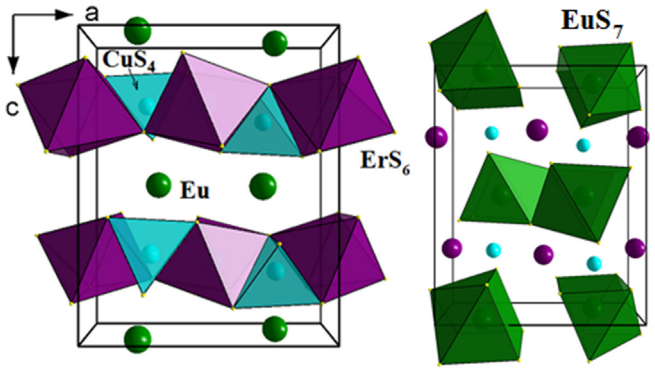

Fig. 2. [010] perspective projections of the $EuErCuS_3$ structure.

Table 2
Atomic coordinates in the $EuErCuS_3$ structure.

Atom	Wyck.	Site	x	y	z
Eu	4c	.m.	0.76479(16)	0.25	0.00169(9)
Er	4c	.m.	0.01020(11)	0.25	0.74489(9)
Cu	4c	.m.	0.24037(24)	0.25	0.22147(14)
S1	4c	.m.	0.05556(47)	0.25	0.11536(34)
S2	4c	.m.	0.42054(49)	0.25	0.10848(35)
S3	4c	.m.	0.25808(44)	0.25	0.82710(28)

tried these calculations for $EuErCuS_3$ in view of problematic valence states of metal ions. To our surprise, the conformity in the case of this specific material appeared to be almost perfect. According to our bond valence sum calculations with the parameters outlined in Ref. [49] as presented in Table 5, the valence states of Eu, Er and Cu ions in $EuErCuS_3$ are close to 2, 3 and 1, respectively. Later the optical evidence for valence state of RE ions will be discussed.

A $EuErCuS_3$ powder consists of planar particles with linear sizes of 1–10 μm (Fig. 3). Energy dispersive X-ray spectrometric analysis was performed at 5 different locations on the sample surface. The chemical composition of the sample agrees with the theoretical contents of the elements.

3.2. Thermal properties and microhardness

The DSC heating curves for a polycrystalline $EuErCuS_3$ sample feature three endotherms in the range 1524–1610 K induced by first-order phase transformations, namely, polymorphic transitions (Fig. 3). Similar transitions were detected in $ALnCuS_3$ (A = Sr or Eu) isostructural compounds [8,18]. The polymorphs of the compound are denoted in the increasing order of temperatures like in the case of $EuErCuS_3$. The temperatures and enthalpies of phase transitions, determined by the heating curves, are listed in the Table 6.

The phase transitions occur within a narrow temperature range less than 10 K. The thermal features are completely reproduced upon cooling, so the transitions may be regarded to be rapid. Quenching of samples to aqueous NaCl solutions failed to yield high-temperature phases of the compound.

Table 4
Selected bond angles in the $EuErCuS_3$ structure.

Angle	ω, deg	Angle	ω, deg
$S1^{i}$—Eu—$S1^{ii}$	71.83(11)	$S1^{iv}$—Er—$S2^{v}$	88.34(10)
$S1^{i}$—Eu—$S2^{ii}$	139.01(7)	$S1^{iv}$—Er—$S2^{xi}$	178.90(14)
$S1^{i}$—Eu—$S3^{iii}$	74.83(11)	$S1^{iv}$—Er—S3	88.20(12)
$S1^{ii}$—Eu—$S1^{viii}$	79.39(11)	$S1^{iv}$—Er—$S3^{vi}$	89.76(12)
$S1^{ii}$—Eu—$S2^{ii}$	74.13(11)	$S2^{v}$—Er—$S2^{xi}$	92.06(14)
$S1^{ii}$—Eu—$S2^{viii}$	122.99(12)	$S2^{v}$—Er—S3	90.77(12)
$S1^{ii}$—Eu—$S3^{iii}$	89.37(9)	$S2^{v}$—Er—$S3^{vi}$	91.25(12)
$S1^{ii}$—Eu—$S3^{ix}$	146.64(13)	S3—Er—$S3^{vi}$	177.09(9)
$S2^{ii}$—Eu—$S2^{viii}$	79.63(12)	S1—Cu—S2	105.28(18)
$S2^{ii}$—Eu—$S3^{iii}$	82.7(1)	S1—Cu—$S3^{vii}$	109.97(13)
$S2^{ii}$—Eu—$S3^{ix}$	136.17(13)	S2—Cu—$S3^{vii}$	110.51(13)
$S3^{iii}$—Eu—$S3^{ix}$	82.98(10)	$S3^{vii}$—Cu—$S3^{xii}$	110.50(16)
$S1^{iv}$—Er—$S1^{x}$	91.24(14)		

Table 5
Bond valence calculations for Eu, Er and Cu in $EuErCuS_3$.

Bond	Dist., Å	R, Å	B	BVal
Eu—S3	2.953	2.584	0.37	0.369
Eu—S3	2.953	2.584	0.37	0.369
Eu—S2	3.055	2.584	0.37	0.280
Eu—S2	3.055	2.584	0.37	0.280
Eu—S1	3.063	2.584	0.37	0.274
Eu—S1	3.063	2.584	0.37	0.274
Eu—S1	3.281	2.584	0.37	0.152
Sum				1.998
Er—S3	2.709	2.460	0.37	0.510
Er—S3	2.718	2.460	0.37	0.498
Er—S2	2.718	2.460	0.37	0.498
Er—S2	2.718	2.460	0.37	0.498
Er—S1	2.737	2.460	0.37	0.473
Er—S1	2.737	2.460	0.37	0.473
Sum				2.950
Cu—S1	2.311	1.898	0.37	0.328
Cu—S2	2.327	1.898	0.37	0.314
Cu—S3	2.381	1.898	0.37	0.271
Cu—S3	2.381	1.898	0.37	0.271
Sum				1.183

The $EuErCuS_3$ compound is formed in EuS-$CuErS_2$ quasi-binary section in Cu_2S–Er_2S_3-EuS triangle. $EuErCuS_3$ compound melts incongruently. According to the XRD and SEM data, the single-phase samples of compound $EuErCuS_3$ having been crystallized from the melt during DSC were found to change into the three-phase compounds. The microstructure of the sample contains primary brown crystals of the phase of EuS (H = 1300 MPa) surrounded by the $EuErCuS_3$ phase crystals being of light brown colour (H = 2850 MPa). In the sample the eutectic consisting of elongated grains of the $EuErCuS_3$ and $CuErS_2$ phases was observed between the grains of the $EuErCuS_3$ phase. The diffraction peaks of all phases were detected on a diffraction pattern. The temperature of incongruent melting of the compound with change in composition of the samples remains constant. The Tamman triangle indicates that thermal effect of incongruent melting belongs to $EuErCuS_3$ compound. This phase transformation scheme, i.e. $EuErCuS_3$ (cr.) ⇄ EuS

Table 3
Interatomic distances (d) in the $EuErCuS_3$ structure.

Bond	d, Å	Bond	d, Å	Bond	d, Å
Eu—$S1^{i}$	3.2800(49)	Er—$S1^{iv}$	2 × 2.7372(32)	Cu—S1	2.312(5)
Eu—$S1^{ii}$	2 × 3.0629(37)	Er—$S2^{v}$	2 × 2.7181(33)	Cu—S2	2.328(5)
Eu—$S2^{ii}$	2 × 3.0552(39)	Er—S3	2.7174(45)	Cu—$S3^{vii}$	2 × 2.3810(23)
Eu—$S3^{iii}$	2 × 2.9529(29)	Er—$S3^{vi}$	2.7093(45)	‹Cu—S›	2.350(2)
‹Eu—S›	3.060(2)	‹Er—S›	2.723(2)		

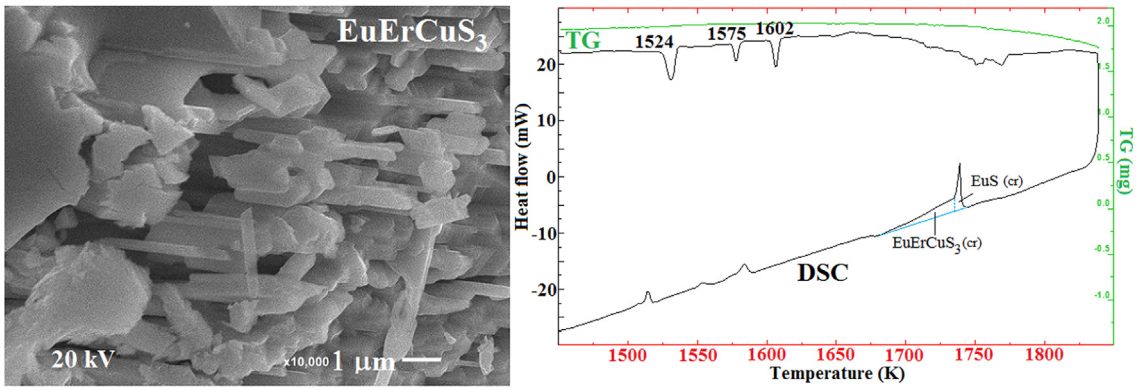

Fig. 3. SEM micrograph and thermal curves for a $EuErCuS_3$ sample. The DSC curve is black, the TG curve is green. (For interpretation of the references to color in this figure legend, the reader is referred to the Web version of this article.)

Table 6
Physicochemical characteristics of $EuErCuS_3$.

Temperatures (K) and enthalpies ($kJ \cdot mol^{-1}$) of phase transitions								
$T_{\alpha\leftrightarrow\beta}$	$\Delta H_{\alpha\leftrightarrow\beta}$	$T_{\beta\leftrightarrow\gamma}$	$\Delta H_{\beta\leftrightarrow\gamma}$	$T_{\gamma\leftrightarrow\delta}$	$\Delta H_{\gamma\leftrightarrow\delta}$	T_{cr}	ΔH_{cr}	
1524 ± 2	2.3 ± 0.2	1575 ± 3	0.7 ± 0.1	1602 ± 3	1.3 ± 0.1	1735 ± 10[a]	−3.5 ± 0.3[a]	
$\chi_{obs} \cdot 10^7$, $m^3 \cdot mol^{-1}$	$C \cdot 10^4$, $m^3 \cdot K \cdot mol^{-1}$		Band gap, eV		Sample colour	H,MPa	T_c,K	
	obs	calc	obs	calc			obs	calc
7.99	2.45	2.43	1.934	2.56	Red-brown	2850 ± 150	4.8 ± 0.2	5.0

[a] As shown by DSC cooling curves.

(cr.) + l is indicative of incongruent melting. Since the thermal effect of incongruent melting on the heating curve is blurry, both the temperature of the starting phase transition and the enthalpy were determined from the cooling curve. The exothermic effect of the solidification, produced in the course of cooling ($\Delta H = -9.8\ J \cdot g^{-1}$), was tentatively divided into two peaks ($\Delta H = -2.6$ J/g и $\Delta H = -7.2\ J \cdot g^{-1}$). The first exothermic peak, turning up in the temperature interval 1735–1740 K characterizes the formation of the primary crystals EuS ($\Delta H = -0.5\ kJ \cdot mol^{-1}$), the second thermal effect shows the result of interaction of the formed crystals EuS with the liquid with the formation of the $EuErCuS_3$ compound ($\Delta H = -3.5\ kJ \cdot mol^{-1}$). Since under cooling we can observe the supercooling effect, the temperature data concerning this phase transition are given tentatively.

The microhardness value measured for $EuErCuS_3$ (Table 6) exceeds the microhardness of isoformula compounds (for $EuLaCuS_3$, H = 2050 MPa [17]), in correlation with the decreasing Ln^{3+} radii.

3.3. Magnetic properties

The 298 K magnetic moment of the test sample rises linearly with field intensity, a trend typical of a paramagnetic state (Fig. 4). The molar magnetic susceptibility χ was calculated from the plot (Fig. 4, Table 6).

The temperature-dependent magnetic susceptibility below 14 K shows a transition to an ordered anisotropic magnetic structure at 4.8 ± 0.2 K (Fig. 5). The reciprocal magnetic susceptibility near the phase transition departs from the linear trend; this departure is typical for ferrimagnets and correlates with a similar behavior observed for $EuGdCuS_3$ (where the transition temperature is 5.37 K [13]).

In Néel' theory, the temperature-dependent reciprocal magnetic susceptibility for a two-sublattice ferrimagnet is described by the relationship [50].

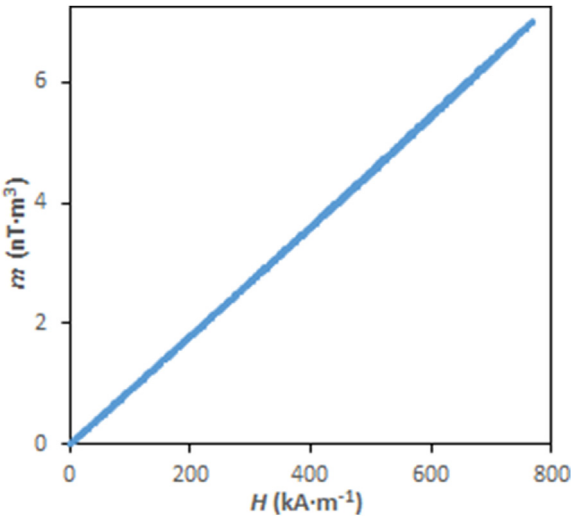

Fig. 4. Magnetic moment versus magnetic field for $EuErCuS_3$.

$$\frac{1}{\chi} = \frac{T}{C} + \frac{1}{\chi_0} - \frac{\sigma}{T-\theta} \quad (1)$$

where C is the Curie constant; and χ_0, σ, and θare the fitting parameters (including C).

Processing of the experimental data (Fig. 5) gave a value of $2.45 \cdot 10^{-4}\ m^3\ K\ mol^{-1}$ for C (for $EuGdCuS_3$, $C = 1.95 \cdot 10^{-4}\ m^3\ K\ mol^{-1}$ [13]). The relationship $C = \mu_0 \frac{N_A}{3k}(\mu_{Eu}^2 + \mu_{Er}^2)$ (whereμis the magnetic moment equal to $7.94\mu_B$ and $9.58\mu_B$ for Eu^{2+} and Er^{3+}, respectively [51,52]) gave $C = 2.43 \cdot 10^{-4}\ m^3\ K\ mol^{-1}$ for the paramagnetic state of $EuErCuS_3$. The thus-calculated values of the Curie constant were used

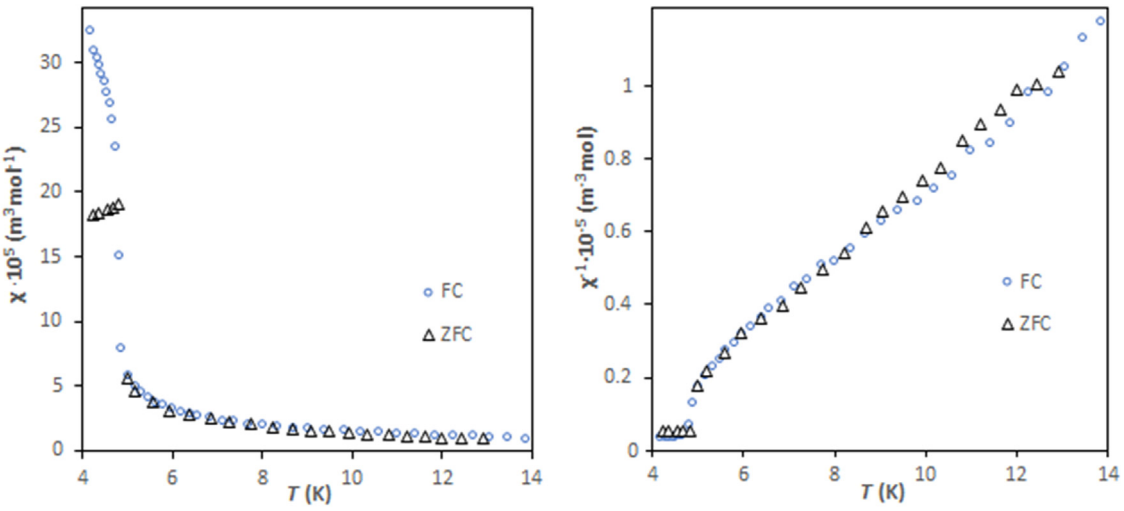

Fig. 5. Temperature-dependent reciprocal magnetic susceptibility for a $EuErCuS_3$ sample.

to calculate χ for 298 K: $8.23 \cdot 10^{-7}$ and $8.19 \cdot 10^{-7}$ m^3 mol^{-1}; these χ values coincide, to within 3%, with the experimentally determined value $\chi = 7.99 \cdot 10^{-7}$ m^3 mol^{-1} (for $EuGdCuS_3$, $\chi \approx 6.3 \cdot 10^{-7}$ m^3 mol^{-1} [13]). The calculations of the Curie temperature (at which $\frac{1}{\chi} = 0$) through the parameters (C, χ_0, σ, and θ)of model (1) by the relationship (2) give $T_c = 5.0$ K.

$$T_c = \theta - \frac{C}{\chi_0} + \frac{1}{2}\sqrt{\left(\theta - \frac{C}{\chi_0}\right)^2 + 4C\left(\frac{\theta}{\chi_0} + \sigma\right)} \quad (2)$$

3.4. Vibrational spectroscopy

Fig. 6 shows Raman spectra recorded at various excitation wavelengths. The noticeable differences between the observed spectra indicate that luminescence spectra were recorded together with the vibrational spectrum. The joint analysis of these spectra makes it possible to exclude the luminescence contribution and recognize the lines that reliably belong to the vibrational frequencies of the crystal unit cell.

Selection rules were calculated for interpreting the observed vibrational spectra. The result is shown in Table 7. The crystal belongs to space group *Pnma*. According to the calculations, 36 modes were expected to appear in the Raman spectrum and 27 modes in IR absorption spectra.

Referring to Fig. 6, we note that luminescence contribution observed in the range above 310 cm^{-1} under 514.5 nm excitation is easily assignable to the transition from excited electronic energy level $^2H_{11/2}$ of Er^{3+} ion to the ground state. Luminescence from $^4S_{3/2}$ and $^4F_{9/2}$ levels of Er^{3+} ion is also detected though it is positioned outside the Raman spectrum region and is visible in Fig. 6., while no detectable luminescence from excited states of Eu^{3+} ion were observed. Under 457.9 nm excitation, Raman peaks are preserved in the spectrum, while $^2H_{11/2}$ peaks completely disappear. On the contrary, for 457.9 nm excitation, the luminescence from $^4F_{7/2}$ state of Er^{3+} ions is in the low wave number part of Raman spectrum. Presence of luminescence from several Er3+ excited levels This is

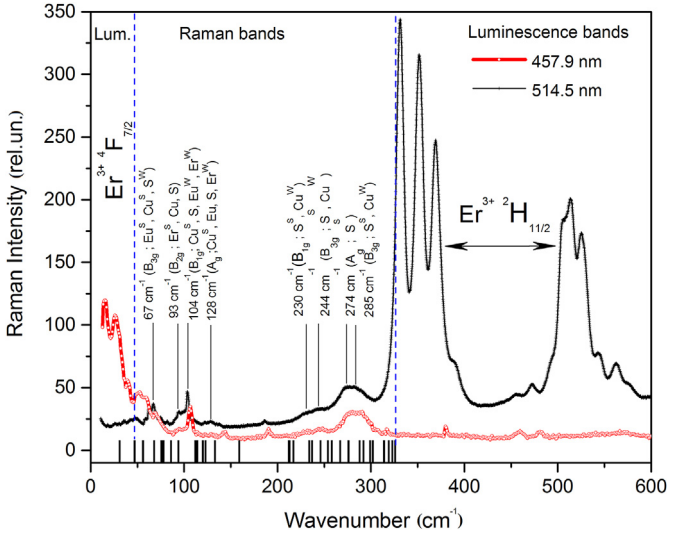

Fig. 6. Raman and luminescence spectra of the $EuErCuS_3$ crystal excited by 514.5- and 457.9-nm laser beams. The bars indicate the calculated Raman frequencies of $EuErCuS_3$.

Table 7
Irreducible representations, classification of modes, and Raman tensors for $EuErCuS_3$ (space group *Pnma*, No.62).

Atom	Phonon modes at point G
Eu	2Ag + Au + B1g+2B1u+2B2g + B2u + B3g+2B3u
Er	2Ag + Au + B1g+2B1u+2B2g + B2u + B3g+2B3u
Cu	2Ag + Au + B1g+2B1u+2B2g + B2u + B3g+2B3u
S	2Ag + Au + B1g+2B1u+2B2g + B2u + B3g+2B3u
S	2Ag + Au + B1g+2B1u+2B2g + B2u + B3g+2B3u
S	2Ag + Au + B1g+2B1u+2B2g + B2u + B3g+2B3u

Classification of modes

$G_{ram} = 12A_g + 6B_{1g} + 12B_{2g} + 6B_{3g}$
$G_{ir} = 11B_{1u} + 5B_{2u} + 11B_{3u}$ (acoustic modes are not included)
$G_{ac} = B_{1u} + B_{2u} + B_{3u}$
$G_{meh} = 12A_g + 6A_u + 6B_{1g} + 12B_{1u} + 12B_{2g} + 6B_{2u} + 6B_{3g} + 12B_{3u}$

Raman tensors

$A_g \begin{bmatrix} 0 & d & 0 \\ d & 0 & 0 \\ 0 & 0 & 0 \end{bmatrix}$ $B_{1g} \begin{bmatrix} 0 & 0 & e \\ 0 & 0 & 0 \\ e & 0 & 0 \end{bmatrix}$ $B_{2g} \begin{bmatrix} 0 & 0 & 0 \\ 0 & 0 & f \\ 0 & f & 0 \end{bmatrix}$ $B_{3g} \begin{bmatrix} a & 0 & 0 \\ 0 & b & 0 \\ 0 & 0 & c \end{bmatrix}$

Lattice dynamics calculations were performed for providing the full-value interpretation of the observed vibrational spectra.

the spectroscopic evidence of the purity of valence states Er^{3+} and Eu^{2+} earlier derived from the XRD data.

3.5. Ab initio lattice dynamics calculations and the interpretation of observed vibrational spectra

The types of phonon modes were determined and the involvement of ions in vibrational modes was evaluated based on the displacement vectors derived from ab initio calculations (Tables 8–10). In the IR spectrum (Table 8), rare-earth ions are appreciably involved in low-frequency modes. Europium is involved in the modes with frequencies up to 133 cm^{-1}. The B_{2u} mode at 93 cm^{-1} involves both Eu and Er. Erbium is involved in the modes with frequencies of up to 145 cm^{-1}. Copper vibrations appear in the IR modes with frequencies of up to 294 cm^{-1}. The greatest involvement of copper is in the 117.6 cm^{-1}(B_{1u}), 118.1 cm^{-1}(B_{2u}), and 129 cm^{-1} (B_{3u}) modes. Sulfur is involved in all IR modes. The 320.5 cm^{-1}(B_{1u}) and 324 cm^{-1} (B_{3u}) high-frequency IR modes mostly arise from sulfur vibrations. Three more modes can be distinguished at 243, 245, and 258 cm^{-1} (B_{2u}, $B_{1u,}$ and $B_{3u,}$ respectively), also arising from sulfur vibrations. Thus, the IR modes that arise from sulfur vibrations can be solely distinguished. For other ions, such modes are difficult to distinguish; every mode involves several ions of different types. For example, the low-frequency IR mode (B_{3u}, 62 cm^{-1}) involves all ions (Eu, Er, Cu, and S), and it is difficult to distinguish the dominant contribution from any one of them. However, this mode has a low intensity. According to the calculations, the 212.9 cm^{-1} (B_{2u}), 213.4 cm^{-1} (B_{3u}), and 259 cm^{-1} (B_{1u}) modes have high intensities. Sulfur is substantially involved in these modes.

According to the calculations, the lowest-frequency Raman mode (A_g, 31 cm^{-1}) considerably involves erbium and europium (Table 9), i.e. considerable involvement of erbium is in the first four low-frequency modes at 31 cm^{-1} (A_g), 47 cm^{-1} (A_g), 56 cm^{-1} (B_{1g}), and 67.8 cm^{-1} (B_{3g}) and in two higher frequency B_{2g} modes at 95 and 160 cm^{-1}, while in the Raman modes with frequencies higher than 160 cm^{-1}, involvement of erbium is insignificant. Europium is strongly involved in the modes with frequencies of up to 86 cm^{-1}; its involvement in higher-frequency modes is far weaker and is insignificant only below 160 cm^{-1}. Thus, both erbium and europium appear in the modes with frequencies of up below 160 cm^{-1}. Europium is the major participant in the B_{3g} mode at 67 cm^{-1} (Fig. 6), while in the B_{2g} mode at 93 cm^{-1}, erbium is strong. A considerable involvement of copper is in the modes with frequencies of up to 128 cm^{-1}. In the modes with frequencies higher than 218 cm^{-1}, copper involvement is weak. Sulfur is involved in all Raman modes. However, modes dominated by sulfur ions appear at 230 cm^{-1} (B_{1g}), 244 cm^{-1} (B_{3g}), 274 cm^{-1} (A_g), 284 cm^{-1} (B_{3g}).

The A_u modes, which are IR- and Raman-inactive, were also obtained by the calculations (Table 10). In the low-frequency A_u mode (68.5 cm^{-1}), involvement of erbium considerable; erbium is also involved in the third lowest frequency mode (111 cm^{-1}). In the 80.5-cm^{-1} mode europium appears. The A_u modes with frequencies higher than 111 cm^{-1} almost do not involve rare-earth ions, however, the involvement of sulfur is considerable.

A comparison of the vibrational frequencies of Raman- and IR-active modes calculated in terms of DFT with the B3LYP functional with the experimental data appear in Figs. 6 and 7.

The calculated IR absorption spectrum corresponds with the observed one. The low-frequency IR modes involve all ions (Eu, Er, Cu, and S), and it is difficult to distinguish the dominant contribution from any one of them. The strongest lines, according to the calculations, are related to sulfur vibrations and appear in the range from 210 to 260 cm^{-1}. The low-frequency Raman vibrations are also related to the vibrations of all ions (lattice vibrations). The vibrations in the range 67–300 cm^{-1} have been identified. According to the calculations, the high-frequency modes are associated with strong displacements of sulfur ions, so the high-frequency vibrations that emerge in the observed spectrum in the range 230–300 cm^{-1} are assigned to the vibrations of sulfur ions.

3.6. Electronic structure calculations and bandgap measurement

The band structure and the density of states obtained in terms of DFT with the B3LYP functional are shown in the Fig. 8. The path in the Brillouin zone is plotted through the most highly symmetric points for the orthorhombic lattice. The path is made through Γ-X-Z-U-Y-S-T-R-Γ. The coordinates of points are (0,0,0), (1/2,0,0), (0,0,1/2), (1/2,0,1/2), (0,1/2,0), (1/2,1/2,0), (0,1/2,1/2), (1/2,1/2,1/2), (0,0,0) respectively. Bilbao Crystallographic Server was used. Since for europium and erbium pseudo-potentials that replaced their core shells including 4f were used the band structure do not include 4f states. The bandgap was calculated to be 2.56 eV. The bandgap was defined as the difference in energy between the top of the valence band and the bottom of the conduction band (it is "HOMO-LUMO" gap). The bandgap is direct (Γ-Γ). The calculation was carried out for the ideal crystal structure. In this case the *f*- orbitals of rare-earth ions were replaced by a pseudopotential. The difference between the measured (1.934 eV) and calculated (2.56 eV) forbidden gap values may be due to these facts. (The impurity of Er_2O_2S (1%) is present in the sample. According to experimental data, the band gap value of Er_2O_2S is about 4 eV [53]. Therefore the difference between the measured and calculated band gap values cannot be explained by the presence of this impurity.)

The projected DOS onto the whole set of atomic orbitals of an Eu,

Table 8
Calculated IR vibrational frequencies (ν_{calc}, cm^{-1}) and intensities (I_{calc}, km/mol) in $EuErCuS_3$.

Vibrations	ν_{calc}	I_{calc}	Involved ions	Vibrations	ν_{calc}	I_{calc}	Involved ions
B_{3u}	62	36,09	Eu, Er, Cu, S1, S2, S3	B_{2u}	243	640,72	S1, $S2^S$
B_{1u}	65	1,82	Eu^S, S1, S2	B_{1u}	245	69,05	$S1^S$, S2,S3
B_{2u}	93	11,69	Eu^S, Er^S, Cu, $S2^W$, S3	B_{3u}	258	506,11	S1, S2, $S3^S$
B_{3u}	100	28,43	Eu, Er, Cu, S1, S2,S3	B_{1u}	259	1447,84	Er^W,Cu^W,S1,S2,S3
B_{3u}	105	62,48	Eu^S, Er, Cu, S1, S2, S3	B_{3u}	269	37,9	Cu,S1, S2,$S3^S$
B_{1u}	112	25,84	Er, Cu, S1, S2, $S3^W$	B_{1u}	279	106,85	Cu, S1, S2,$S3^S$
B_{1u}	117,6	0,18	Eu, Er, Cu^S, S1, S2	B_{3u}	290	0,62	Cu, S1, $S2^S$,S3
B_{2u}	118,1	47,99	Eu, Cu^S, S3	B_{2u}	294	251,33	Cu,$S3^S$
B_{3u}	123,6	10,73	Eu, Cu, S1, S2	B_{1u}	300	10,08	S1, $S2^S$,$S3^S$
B_{3u}	129	148,97	Er, Cu^S, S1, S2,S3	B_{1u}	309	20,55	Cu^W, $S1^S$, S2, S3
B_{1u}	133	430,77	Eu^S, Er, Cu, S1, S2	B_{3u}	311	14,18	Cu^W, S1, $S2^S$, S3
B_{1u}	145	1,66	Er^S, S1, S2,S3	B_{1u}	320,5	12,41	S1, S2,$S3^S$
B_{2u}	212,9	1950,47	Er^W, S1, S2	B_{3u}	324	0,16	$S1^S$, S2,$S3^S$
B_{3u}	213,4	2113,62	Er^W, Cu^W, S1, S2,S3				

Notations: «s» stands for a strong and «w» for a weak displacement of ions involved in the mode.

Table 9
Calculated Raman vibrational frequencies (v_{calc}, cm^{-1}) in $EuErCuS_3$.

Vibrations	v_{calc}	Involved ions	Vibrations	v_{calc}	Involved ions
A_g	31	Eu^S, Er^S, Cu, S1, $S2^S$,S3	B_{3g}	216,5	$S1^S$, S2
A_g	47	Eu, Er^S, Cu^S, S1, S2,$S3^S$	B_{1g}	216,6	$S1^S$, S2,S3
B_{1g}	56	Er^S, Cu, S1, S2,S3	A_g	218	Er^W, Cu, $S1^S$, $S2^S$,S3
B_{3g}	67,8	Eu, Er^S, Cu, S1, S2,S3	B_{1g}	246	S1, $S2^S$
A_g	76	Eu^S, Er^W, Cu^S, S1, S2,S3	B_{2g}	247	Cu^W, $S1^S$, S2,S3
B_{3g}	77	Eu^S, Er, Cu, S1, $S2^W$,S3	B_{3g}	249	S1, $S2^S$
B_{2g}	79	Eu^S, Er, Cu^W, S1, S2,S3	B_{2g}	255	Cu^W, S1, $S2^S$,S3
B_{1g}	80,3	Eu^S,Cu, S1, $S2^W$, S3	A_g	257	S1, S2,$S3^S$
B_{2g}	86	Eu^S, S2	A_g	270	Cu, S1, $S2^W$,$S3^S$
B_{2g}	95	Er^S, Cu, S1, S2,S3	A_g	277	$S1^S$, $S2^S$
B_{1g}	115,8	Eu^w, Er^w, Cu^S,S3	B_{3g}	291	Cu^W,$S3^S$
B_{2g}	116,3	Er^w, Cu^S,S2	B_{1g}	296	Cu^W,$S3^S$
B_{3g}	117,9	Eu, Cu^S,S3	B_{2g}	302	Cu^W, S1, $S2^S$,$S3^S$
A_g	122	Eu, Er, Cu, S1, S2	B_{2g}	303	$S1^S$, S2,$S3^S$
B_{2g}	123,9	Cu^S, $S1^S$, S3	A_g	317	Cu^W, S1, $S2^S$,S3
A_g	128	Eu, Er^W, Cu^S, S2,S3	B_{2g}	320,7	$S1^S$, S2,$S3^S$
A_g	137	Eu, Er, Cu, S1, S2	A_g	325	$S1^S$, S2,S3
B_{2g}	160	Eu, Er^S, $S1^W$, $S2^W$	B_{2g}	328	Cu^W, S1, $S2^S$,S3

Table 10
Vibrational frequencies (v_{calc}, cm^{-1}) of Raman silent modes in $EuErCuS_3$.

Vibrations	v_{calc}	Involved ions
A_u	68,5	Er^S, Cu^W, S1, S2, $S3^W$
A_u	80,5	Eu^S, Er^W, Cu, $S2^W$, S3
A_u	111	Eu, Er^S, S3
A_u	211	$S1^S$, S2, S3
A_u	244	$S1^S$, S2
A_u	292	Cu^W, $S3^S$

Er, Cu and S atoms was calculated near to bandgap (Fig. 8C). According to the calculations, the DOS of sulfur locate near to top of valence band and bottom of conduction band. The DOS of rare-earth and copper locate near to top of valence band. $EuErCuS_3$ is a mid-gap, direct-bandgap semiconductor.

Fig. 9 presents Kubelka-Munk function determined according to the measured diffuse reflection spectrum of $EuErCuS_3$. The agreement between the experimental value of E_g and the calculated one is not perfect, however, it can be considered as a satisfactory one. Additionally, the position of $H_{13/2}$ energy level of Er^{3+} ion within the bandgap can be identified from the data of reflectance spectra. This energy level is observable as the narrow peak at the left side of Kubelka-Munk function, and the maximum of this peak is at 1.546 μm (6468 cm^{-1}), approximately in the same region where luminescence of Er ion is observed in oxides [54].

4. Conclusions

This article addresses the synthesis, structure, optical, magnetic, durometric, and thermal properties of the new complex sulfide $EuErCuS_3$. The compound crystallizes in a Eu_2CuS_3-type structure, which is typical for the $EuLnCuS_3$ compounds that contain mid-series lanthanides ranged from samarium to erbium. $EuErCuS_3$, which contains the magnetic ion Er^{3+}, experiences a ferrimagnetic transition at 4.8 K. The compound manifests three reversible polymorphic transitions in the temperature range 1524–1720 K. It crystallizes at 1735K. The magnetic and thermal properties of $EuErCuS_3$ are compliant with the data published for the $ALnCuS_3$ (A = Sr, Eu; Ln = La–Lu) isostructural compounds [8,13,14]. Ab initio crystal structure and phonon spectrum calculations have been performed for $EuErCuS_3$ in terms of the LCAO-MO approach and density functional theory with the use of the B3LYP hybrid functional. The results of the calculations enabled us to interpret the observed vibrational spectra. Valence state of RE ions (Er3+ and Eu2+) was checked by combination of XRD and luminescence spectroscopy. Optical band gap was found to be 1.934 eV from diffuse reflectance spectrum. The difference between the measured and calculated values may be due to the fact that in the calculations the f- orbitals of the rare-earth ions were replaced by a pseudo-potential. The calculation was carried out in order to reproduce the dynamics of the crystal lattice. For this purpose this approach is fully justified. Moreover, the calculation was carried out for an ideal crystal structure.

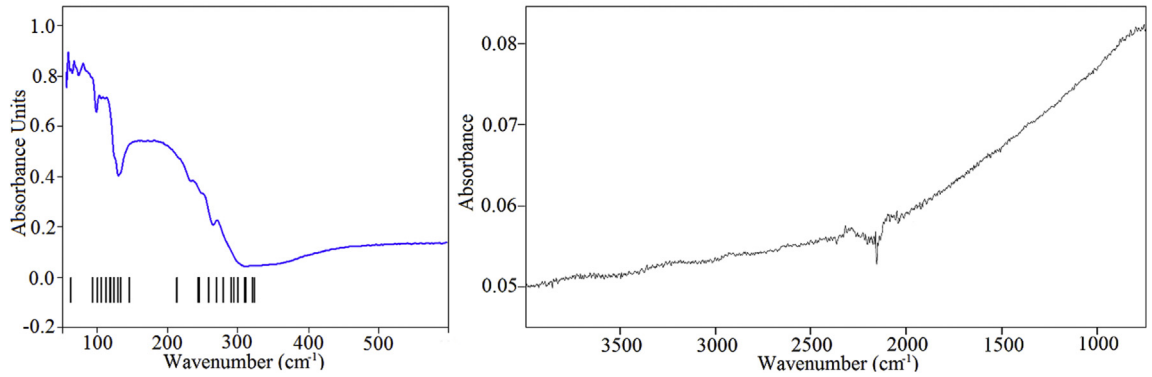

Fig. 7. IR spectrum of $EuErCuS_3$. The bars indicate the calculated IR vibrational frequencies in $EuErCuS_3$. $EuErCuS_3$ is IR-transparent in the wave number window 4000–400 cm^{-1}.

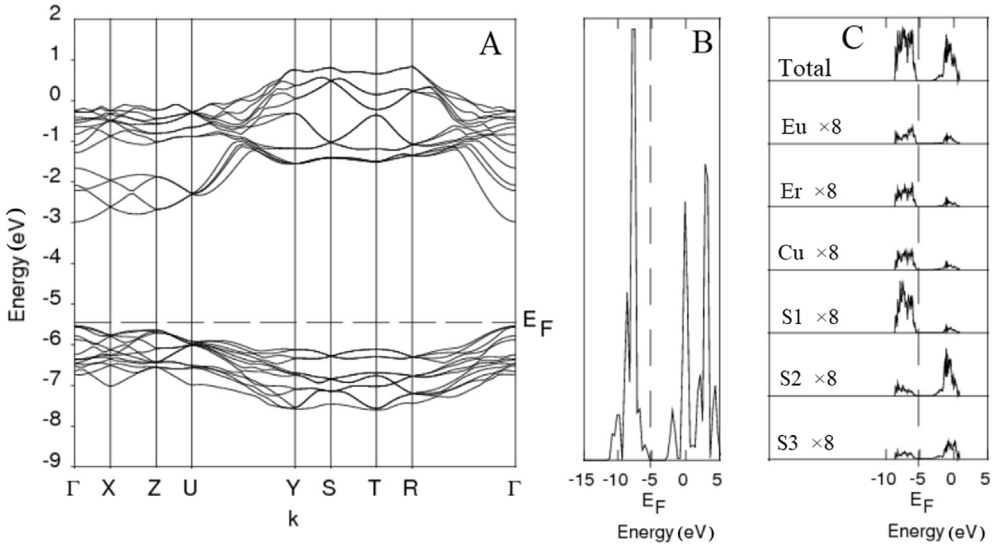

Fig. 8. $EuErCuS_3$ band structure and the density of states.

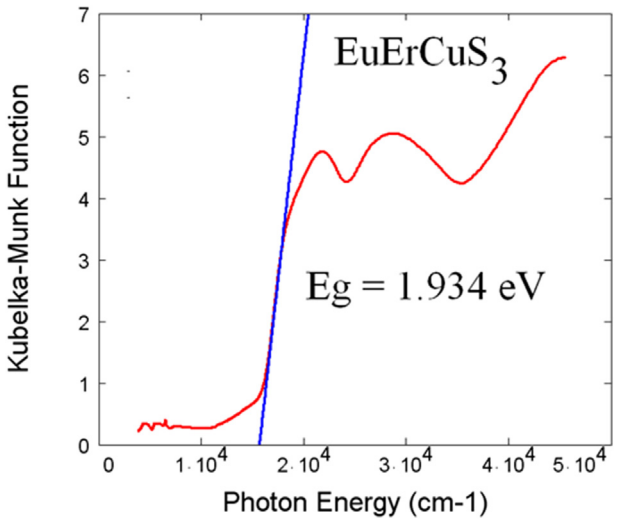

Fig. 9. Diffuse reflection spectra of $EuErCuS_3$.

Vibrational modes of $EuErCuS_3$ lattice are identified in the experimental Raman spectrum.

Author contributions

All authors reviewed and commented on the manuscript.

Acknowledgements

The work was supported by the State budget allocated to the fundamental research in the Ministry of Science and Education, Russian Federation of (Project No. V.45.3.3); by RFBR Grant 17-02-00754; by the Ministry of Science and Higher Education of the Russian Federation under Project No 3.9534.2017/8.9.

References

[1] L.D. Gulay, M. Daszkiewicz, V Ya Shemet, A. Pietraszko, Crystal structure of the R_2PbS_4 (R = Yb and Lu) compounds, J. Alloy. Comp. 453 (2008) 143–146, https://doi.org/10.1016/j.jallcom.2006.11.110.
[2] L.D. Gylay, I.D. Olekseyuk, M. Wolcyrz, J. Stepien-Damm, Crystal structures of the $RCuPbS_3$ (R = Tb, Dy, Ho, Er, Tm, Yb and Lu) compounds, J. Alloy. Comp. 399 (2005) 189–195, https://doi.org/10.1016/j.jallcom.2005.03.036.
[3] L.A. Koscielski, J.A. Ibers, The structural chemistry of quaternary chalcogenides of the type $AMM'Q_3$, Z. Anorg. Allg. Chem. 638 (2012) 2585–2593, https://doi.org/10.1002/zaac.201200301.
[4] T.D. Brennan, J.A. Ibers, $LaPbCuS_3$: Cu(I) insertion into the a-La_2S_3 framework, J. Solid State Chem. 97 (1992) 377–382, https://doi.org/10.1016/0022-4596(92)90046-X.
[5] M. Ohta, S. Hirai, T. Mori, Y. Yajima, T. Nishimura, K. Shimakage, Effect of nonstoichiometryon thermoelectric properties of γ-Tb_2S_{3-x}, J. Alloy. Comp. 418 (2006) 209–212, https://doi.org/10.1016/j.jallcom.2005.10.065.
[6] M. Ohta, H. Yuan, S. Hirai, Y. Yajima, T. Nishimura, K. Shimakage, Thermoelectric properties of Th_3P_4-type rare-earth sulfides Ln_2S_3 (Ln = Gd, Tb) prepared by reaction of their oxides with CS_2 gas, J. Alloy. Comp. 451 (2008) 627–631, https://doi.org/10.1016/j.jallcom.2007.04.078.
[7] V.O. Aliev, N.R. Akhmedova, S.M. Agapasheva, O.M. Aliev, Crystal growth and physicochemical properties of structural analogs of krupkaite, Inorg. Mater. 45 (2009) 717–722, https://doi.org/10.1134/S0020168509070024.
[8] A.V. Ruseikina, O.V. Andreev, E.O. Galenko, S.I. Koltsov, Trends in thermodynamic parameters of phase transitions of lanthanide sulfides $SrLnCuS_3$ (Ln = La–Lu), J. Therm. Anal. Calorim. 128 (2017) 993–999, https://doi.org/10.1007/s10973-016-6010-9.
[9] YuA. Murashko, A.V. Ruseikina, A.A. Kislitsyn, O.V. Andreev, Optical and thermal properties of the EuLnCuS3 (Ln = La, Pr, Sm,Gd), Inorg. Mater. 51 (2015) 1213–1218, https://doi.org/10.1134/S0020168515120079.
[10] R.M. Rojas, M.J. Torralvo, L.C. Otero-Diaz, Thermal behaviour and microstructural characterization of lanthanide sulphides, J. Therm. Anal. Calorim. 38 (1992) 961–971. https://doi.org/10.1007/BF01979429.
[11] K. Matsumoto, L. Li, S. Hirai, E. Nakamura, D. Murayama, Y. Ura, S. Abe, Large magnetocaloric effect in sintered ferromagnetic EuS, Cryogenics 79 (2016) 45–48. https://doi.org/10.1016/j.cryogenics.2016.08.001.
[12] A.V. Ruseikina, L.A. Solov'ev, O.V. Andreev, Crystal structures and properties of $SrLnCuS_3$ (Ln = La, Pr), Russ. J. Inorg. Chem. 59 (2014) 196–201, https://doi.org/10.1134/S0036023614030188.
[13] M. Wakeshima, F. Furuuchi, Y. Hinatsu, Crystal structures and magnetic properties of novel rare-earth copper sulfides, $EuRCuS_3$ (R = Y, Gd–Lu), J. Phys. Condens. Matter 16 (2004) 5503–5518, https://doi.org/10.1088/0953-8984/16/30/012.
[14] F. Furuuchi, M. Wakeshima, Y. Hinatsu, Magnetic properties and (151) Eu Mossbauer effects of mixed valence europium copper sulfide Eu_2CuS_3, J. Solid State Chem. 177 (2004) 3853–3858, https://doi.org/10.1016/j.jssc.2004.04.034.
[15] P. Wu, A.E. Christuk, J.A. Ibers, New quaternary chalcogenides $BaLnMQ_3$ (Ln = rare earth; M = Cu, Ag; Q=S, Se). Structure and property variation vs rare-earth element, J. Solid State Chem. 110 (1994) 337–344, https://doi.org/10.1006/jssc.1994.1177.
[16] A.V. Ruseikina, O.V. Andreev, Regularities of change in the structural parameters of $EuLnCuS_3$ (Ln = La–Nd, Sm, Gd, Ho), Russ. J. Inorg. Chem. 62 (2017) 160–167, https://doi.org/10.1134/S0036023617020140.
[17] A.V. Ruseikina, O.V. Andreev, Phase equilibria in the Cu_2S–La_2S_3–EuS system, Russ. J. Inorg. Chem. 62 (2017) 610–618, https://doi.org/10.1134/S0036023617050199.
[18] A.V. Ruseikina, Zh A. Demchuk, Crystal structure and properties of $AHoCuS_3$ (A = Sr or Eu), Russ. J. Inorg. Chem. 62 (2017) 27–32, https://doi.org/10.1134/S0036023617010168.

[19] A.V. Ruseikina, O.V. Andreev, Phase equilibria in systems $DyCuS_2$–EuS and Cu_2S–Dy_2S_3–EuS, Russ. J. Inorg. Chem. 63 (2018) 1494–1500, https://doi.org/10.1134/S0036023618110141.
[20] W. Cook, L. Shiozawa, F. Augustine, The Cu-S phase diagram, J. Appl. Phys. 41 (1970) 3058–3063.
[21] D.J. Chakrabarti, D.E. Laughlin, The Cu-S (Copper-Sulfur) system, Bull. Alloy. Phase Diagrams 4 (1983) 254–271. https://link.springer.com/content/pdf/10.1007/bf02868665.pdf.
[22] L. Li, S. Hirai, E. Nakamura, H. Yuan, Influences of Eu_2O_3 characters and sulfurization conditions on the preparation of EuS and its large magnetocaloric effect, J. Alloy. Comp. 687 (2016) 413–420. https://doi.org/10.1016/j.jallcom.2016.06.053.
[23] L. Li, S. Hirai, H. Yuan, Influences of Yb_2O_3 characters and sulfurization conditions on preparation of Yb_2S_3, J. Alloy. Comp. 618 (2015) 742–749. https://doi.org/10.1016/j.jallcom.2014.08.109.
[24] A.V. Ruseikina, L.A. Solovyov, M.V. Grigoriev, O.V. Andreev, Crystal structure variations in the series $SrLnCuS_3$ (Ln = La, Pr, Sm, Gd, Er and Lu), Acta Crystallogr. C75 (2019) 584–588. https://doi.org/10.1107/S2053229619004984.
[25] T. Schleid, F. Lissner, Einkristalle von A-Nd_2S_3, U-Ho_2S_3, D-Er_2S_3 und E-Lu_2S_3 durch Oxidation reduzierter Chloride der Lanthanide mit Schwefel, Z. Anorg. Allg. Chem. 615 (1992) 19 26. https://doi.org/10.1002/zaac.19926150905.
[26] C.M. Forster, W.B. White, Optical absorption edge in rare earth sesqui sulfides, Mater. Res. Bull. 41 (2006) 448–454. https://doi.org/10.1016/j.materresbull.2005.07.035.
[27] V.A. Obolonchik, L.A. Ivanchenko, Properties of Europium Chalcogenides, Scientific thought, Kiev, 1980.
[28] K.G. Subhadra, Rao B. Raghavendra, D.B. Sirdeshmukh, X-ray determination of the Debye-Waller factors and Debye temperatures of europium monochalcogenides, Pramana - J. Phys. 38 (1992) 681–683, https://doi.org/10.1007/bf02875064.
[29] P.P. Fedorov, Anneal time determined by studying phase transitions in solid binary systems, Russ. J. Inorg. Chem. 37 (1992), 973-968.
[30] J.W. Visser, A fully automatic program for finding the unit cell from powder data, J. Appl. Crystallogr. 2 (1969) 89–95. https://doi.org/10.1107/S0021889869006649.
[31] P. Lemoine, D. Carré, M. Guittard, Structure du Sulfure d'Europium et de Cuivre Eu_2CuS_3, Acta Crystallogr. 42 (1986) 390–391, https://doi.org/10.1107/S0108270186096063.
[32] L.A. Solovyov, Full-profile refinement by derivative difference minimization, J. Appl. Crystallogr. 37 (2004) 743–749, https://doi.org/10.1107/S0021889804015638.
[33] Brandenburg K. Diamond – visual crystal structure information system crustal impact, Post 1251, D-53002 Boon.
[34] A.G. Kolmakov, V.F. Terentyev, M.B. Bakirov, Hardness Measurement Methods, second ed., Intermet Engineering, Moscow, 2005. http://www.pseudology.org/science/Metody_izmer_tverdosti2.pdf.
[35] D.A. Velikanov, Vibration magnetometer. RF patent for the invention № 2341810. Publ. 12.20, 2008, p. 35. Bulletin №, http://www.freepatent.ru/patents/2341810.
[36] D.A. Velikanov, Magnetometer with a superconducting quantum interferometric sensor. RF patent for the invention № 2481591. Publ. 10.05.2013, Bulletin № 13, http://www.freepatent.ru/patents/2481591.
[37] V.G. Tsirelson, Quantum Chemistry. Molecules, Molecular Systems and Solids, third ed., Binom. Knowledge Lab, Moscow, 2014.
[38] A.D. Becke, Density-functional thermochemistry. III. The role of exact exchange, J. Chem. Phys. 98 (1993) 5648–5652, https://doi.org/10.1063/1.464913.
[39] P.L. Stephens, F.J. Devlin, C.F. Chabalowski, M.J. Frisch, Ab initio calculation of vibrational absorption and circular dichroism spectra using density functional force fields, J. Phys. Chem. 98 (1994) 11623–11627, https://doi.org/10.1021/j100096a001.
[40] R. Dovesi, R. Orlando, A. Erba, C.M. Zicovich-Wilson, B. Civalleri, S. Casassa, L. Maschio, M. Ferrabone, M. De La Pierre, P. D'Arco, Y. Noel, M. Causa, M. Rerat, B. Kirtman, Crystal14: a program for the ab initio investigation of crystalline solids, Int. J. Quantum Chem. 114 (2014) 1287–1317, https://doi.org/10.1002/qua.24658.
[41] Crystal. http://www.crystal.unito.it/index.php. (Accessed 29 October 2018).
[42] M. Dolg, H. Stoll, A. Savin, H. Preuss, Energy-adjusted pseudopotentials for the rare earth elements, Theor. Chim. Acta 75 (1989) 173–194, https://doi.org/10.1007/BF00528565.
[43] M. Dolg, H. Stoll, H. Preuss, A combination of quasi relativistic pseudopotential and ligand field calculations for lanthanoid compounds, Theor. Chim. Acta 85 (1993) 441–450, https://doi.org/10.1007/BF01112983.
[44] Energy-consistent Pseudopotentials of the Stuttgart/Cologne Group. http://www.tc.uni-koeln.de/PP/clickpse.en.html. (Accessed 29 October 2018).
[45] K. Doll, N.M. Harrison, Chlorine adsorption on the Cu(111) surface, Chem. Phys. Lett. 317 (2000) 282–289, https://doi.org/10.1016/S0009-2614(99)01362-7.
[46] T. Ouazzani, A. Lichanot, C. Pisani, C. Roetti, Relaxation and electronic structure of surfaces in lithium sulphide: a Hartree-Fockab initio approach, J. Phys. Chem. Solids 54 (1993) 1603–1611, https://doi.org/10.1016/0022-3697(93)90356-V.
[47] V.A. Chernyshev, A.E. Nikiforov, V.P. Petrov, A.V. Serdtsev, M.A. Kaschenko, S.A. Klimin, Structure and lattice dynamics of rare-earth ferroborate crystals: ab initio calculation, Phys. Solid State 58 (2016) 1642–1650, https://doi.org/10.1134/S1063783416080096.
[48] V.A. Chernyshev, V.P. Petrov, A.E. Nikiforov, Lattice dynamics of rare-earth titanates with the structure of pyrochlore $R_2Ti_2O_7$ (R = Gd, Tb, Dy, Ho, Er, Tm, Yb, and Lu): ab initio calculation, Phys. Solid State 57 (2015) 996–1002, https://doi.org/10.1134/S1063783415050078.
[49] N.E. Brese, M. O'Keeffe, Bond-valence parameters for solids, Acta Crystallogr. B47 (1991) 192–197. http://doi.org/10.1107/S0108768190011041.
[50] L. Néel, Magnetism and local molecular field, Science 174 (1971) 985–992, https://doi.org/10.1126/science.174.4013.985.
[51] N.V. Kudrevatykh, A.S. Volegov, Magnetism of Rare Earth Metals and Their Intermetallic Compounds, pub. UralUniversity, Yekaterinburg, 2015. http://elar.urfu.ru/bitstream/10995/36121/1/978-5-7996-1604-5_2015.pdf.
[52] J. Jensen, A.R. Mackintosh, Rare Earth Magnetism. Structures and Excitations, Clarendon Press, Oxford, 1991. https://www.fys.ku.dk/~jjensen/Book/Ebook.pdf.
[53] W. Sun, X. Yang, M. Yu, L. Wang, Q. Zhang, Experimental and theoretical studies on the stable synthesis of a laser protective coating material erbium oxysulfide, J. Mater. Sci. Mater. Electron. 29 (2017) 2406–2415, https://doi.org/10.1007/s10854-017-8159-9.
[54] Xiao Xia Zhang, Fai King, Li Kok, Wai Cheah, Xianju Zhou, Peter A. Tanner. 1.54 and 1.75 μm infrared luminescence of Y_2O_3:Er^{3+}, Chem. Phys. Lett. 400 (2004) 331–335.